Research Article

Yemao Lin#, Jintao Huang#, Ludi Shi, Guangtao Cong*, Caizhen Zhu*, and Jian Xu

Combining $Zn_{0.76}Co_{0.24}S$ with S-doped graphene as high-performance anode materials for lithium- and sodium-ion batteries

https://doi.org/10.1515/ntrev-2020-0091
received October 14, 2020; accepted November 26, 2020

Abstract: An easy and facile hydrothermal method is presented to synthesize hybrid materials of hollow mesoporous $Zn_{0.76}Co_{0.24}S$ nanospheres anchored on reduced graphene oxide (rGO) sheets ($Zn_{0.76}Co_{0.24}S$@N/S-rGO), in which the obtained $Zn_{0.76}Co_{0.24}S$ nanospheres are composed of numerous nanoparticles. Being evaluated as anode materials for lithium-ion batteries (LIBs) and sodium-ion batteries (SIBs), the $Zn_{0.76}Co_{0.24}S$@N/S-rGO composites exhibited a high reversible capacity of 804 and 605 mA h g^{-1} at the current density of 1 A g^{-1} after 500 cycles for LIBs and SIBs, respectively. The excellent electrochemical performance of $Zn_{0.76}Co_{0.24}S$@N/S-rGO composites originates from the synergistic effect between hollow $Zn_{0.76}Co_{0.24}S$ nanospheres and reduction graphene, as well as the void spaces between the neighbouring nanoparticles of $Zn_{0.76}Co_{0.24}S$ providing large contact areas with electrolyte and buffer zone to accommodate the volume variation during the cycling process.

Keywords: $Zn_{0.76}Co_{0.24}S$@N/S-rGO, sodium-ion batteries, lithium-ion batteries, anode materials

1 Introduction

The exhaustion of non-renewable energy sources has brought about a series of environmental problems, which promote the development of innovative energy storage technologies to harvest the clean and sustainable energy [1]. Among various available energy storage technologies, rechargeable batteries play a significant role as power sources which have been widely applied in electric vehicles and various portable electronic devices [2]. Owing to their long lifespan, high power, and energy density, lithium-ion batteries (LIBs) have dominated the world's batteries market for many years [3]. Recently, due to the low cost and ubiquitous sodium resource, sodium-ion batteries (SIBs) have also attracted widespread attention as a promising alternative to LIBs [4]. Due to the high energy density, morphology-controlled, high theoretical capacities (500–1,000 mA h g^{-1}), transition metal sulphides have been widely investigated and used in secondly energy storages [5]. However, currently neither of LIBs and SIBs could fully meet the ever-increasing demand for energy storage systems with high energy density [6]. Therefore, it is critical to develop advanced electrode materials with excellent property both for LIBs and SIBs [7].

One major challenge for both LIBs and SIBs is to develop suitable anode materials with high capacity, low redox potential as well as long cycle life [8]. The large volume change associated with sodiation/desodiation processes leads to the agglomeration of electrode particles along with electrical disconnection from current collectors, resulting in poor cycling stability [9]. As a type of promising anode materials, transitional metal chalcogenides have been attracting significant interests because of their superior conductivity and high theoretical capacity [10]. Nevertheless, there are still several problems that need to be solved before their application in practice, including poor cycle life and low rate performance, which are mainly caused by the serious volume expansion during charge/discharge [11].

# These authors contributed equally to this work.

*** Corresponding author: Guangtao Cong,** Institute of Low-dimensional Materials Genome Initiative, College of Chemistry and Environmental Engineering, Shenzhen University, Shenzhen 518060, China, e-mail: congguangtao@gmail.com
*** Corresponding author: Caizhen Zhu,** Institute of Low-dimensional Materials Genome Initiative, College of Chemistry and Environmental Engineering, Shenzhen University, Shenzhen 518060, China, e-mail: czzhu@szu.edu.cn
Yemao Lin, Jintao Huang, Ludi Shi, Jian Xu: Institute of Low-dimensional Materials Genome Initiative, College of Chemistry and Environmental Engineering, Shenzhen University, Shenzhen 518060, China

Extensive efforts have been conducted to explore new strategies for the design and synthesis of transitional metal chalcogenide anodes with micro/nanostructure [12]. Hollow-structured materials have drawn great attention and proven to be efficient way to accommodate the volume fluctuation of transitional metal chalcogenides during cycling [13]. Such unique structures can not only provide large electrolyte/electrode contact area for rapid ion diffusion and reaction, but also effectively buffer the dramatic volumetric changes during electrochemical reactions. In addition, to improve the electronic conductivity of the metal chalcogenides and enhance the rate performance of the electrodes, electric-conductive, carbon matrix is commonly adopted to fabricate transitional-metal-chalcogenide/C composites [14]. Among numerous carbonaceous materials, graphene has been widely used as an ideal electrochemical matrix, due to its large surface area and outstanding electronic and electrochemical properties [15]. Therefore, the utilization of hollow framework in combination with graphene as conductive carbon material might be a synergistic strategy to address the aforementioned problems.

Herein, we demonstrated a facile and efficient hydrothermal synthesis method to prepare hollow-structured $Zn_{0.76}Co_{0.24}S$ nanospheres anchored on rGO as anodes materials of LIBs and SIBs. The obtained $Zn_{0.76}Co_{0.24}S$@N/S-rGO composite delivers high discharge capacities of 1,265 and 672 mA h g^{-1} at a current density of 0.1 A g^{-1} for LIBs and SIBs, respectively. The remarkable electrochemical performances of $Zn_{0.76}Co_{0.24}S$@N/S-rGO are mainly attributed to the following advantages. First, the mesoporous hollow-structured $Zn_{0.76}Co_{0.24}S$ can provide large specific contact area for electrolyte/electrode contact. Second, the superior electrical conductivity of graphene leads to prominent electronic/ionic diffusion and enhanced structure stability. Third, the *in situ* sulfur doping can not only increase the capacity, but also improve the electrochemical properties of the carbon materials [16].

2 Experimental section

2.1 Synthesis of $Zn_{0.76}Co_{0.24}S$@N/S-rGO and $Zn_{0.76}Co_{0.24}S$ nanospheres

The aqueous suspension of GO was obtained by dispersing graphite flakes into deionized water (via well-known modified Hummers method) and the concentration of GO was 1 mg mL^{-1} [17]. $Zn_{0.76}Co_{0.24}S$@N/S-rGO composite was synthesized through a facile hydrothermal method. In a typical synthesis of $Zn_{0.76}Co_{0.24}S$@N/S-rGO, the GO solution was sonicated for 1 h and then stirred for half an hour. Then 7.6×10^{-4} mol of Zinc nitrate and 2.4×10^{-4} mol of cobalt nitrate hexahydrate were introduced into 35 mL GO solution (solution A). The solution B was prepared by adding 3×10^{-4} mol L-cysteine and another 35 mL GO solution. After mixing solution B into solution A under continuous stirring for an hour, the obtained mixture was then transferred into 100 mL Teflon-lined autoclave for solvothermal at 180°C for 6 h. The black precipitate produced was centrifuged at 8,000 rpm for 5 min and washed with deionized water and absolute ethanol several times, followed by freeze-dried for further use. Then the dried product was calcinated at 400°C at a heating rate of 2°C min^{-1} for 3 h under argon atmosphere to obtain the $Zn_{0.76}Co_{0.24}S$@N/S-rGO composite. Pure $Zn_{0.76}Co_{0.24}S$ nanospheres were prepared with a similar approach above, except the addition of GO.

In this work, $Zn_{0.76}Co_{0.24}S$ nanospheres were uniformly distributed and anchored on N/S-doped reduced graphene oxide (rGO) network through an effective solvothermal method (denoted as $Zn_{0.76}Co_{0.24}S$@N/S-rGO). As illustrated in Scheme 1, GO was dispersed in deionized water and sonicated for half an hour. Then, $ZnNO_3{\cdot}6H_2O$, $CoNO_3{\cdot}6H_2O$ and L-cysteine were dissolved in GO solution and transferred to autoclave and heated at 180°C for 6 h. In the subsequent calcination process, the sulphur atoms derived from the L-cysteine were *in situ* doped in rGO network. The well-dispersed hollow $Zn_{0.76}Co_{0.24}S$ nanospheres were tightly anchored on the GO network.

2.2 Material characterization

The crystal structure and composition information of all samples were analysed with Powder X-ray diffraction (XRD, Bruker D8 Advance X-ray diffractometer) with Cu Kα. The morphology of the obtained samples was characterized by field-scanning electron microscope (FESEM, JEOL 7500F, Japan) and transmission electron microscope (TEM, JEOL JEM-2100F, Japan). Nitrogen sorption isotherms were tested by V-Sorb X800 and X-ray photoelectron spectroscopy (XPS, VG Scientific) was tested to evaluate the valence of Zn, Co S and C.

2.3 Electrochemical measurements

The electrochemical properties of $Zn_{0.76}Co_{0.24}S$@N/S-rGO and $Zn_{0.76}Co_{0.24}S$ were investigated in CR2032 half cells at

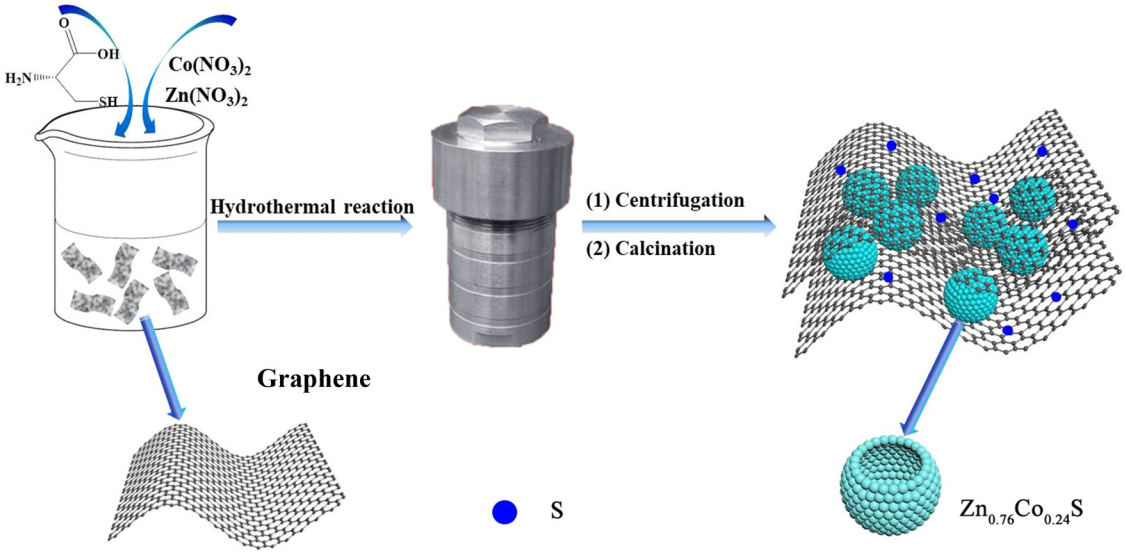

Scheme 1: Schematic illustration of the synthesis procedure of $Zn_{0.76}Co_{0.24}S$@N/S-rGO composites.

ambient temperature. The obtained active materials of $Zn_{0.76}Co_{0.24}S$ @N/S-rGO (70 wt%), acetylene black (20 wt%), and binder sodium alginate (SA) (10 wt%) were dispersed in DI water to form a homogeneous slurry. Then the obtained slurry was pasted on a copper foil, followed by vacuum drying at 110°C for 12 h. The copper discs with a diameter of 14 mm were punched out of copper foil and used as working electrode. The mass loading of active materials on cooper film was found to be about 1.5 mg cm^{-2}. For lithium batteries, the CR2032 coin cells were assembled in an argon-filled glovebox (UniLab, MBRAUN, Germany) with both moisture and oxygen levels below 0.1 ppm. $LiPF_6$ solution (1 M in mixed EC/DMC/EMC, in a volume ratio of 1:1:1) and a pure lithium foils were used as electrolyte and the counter electrode, respectively. For sodium batteries, 1.25 M $NaPF_6$ dissolved in ethyl methyl carbonate (EMC) were used as electrolyte and sodium foil was used as the counter electrolyte. Cyclic voltammetry (CV) was conducted in a CHI 660D electrochemical workstation within a voltage of 0.01–3.0 V at 0.1 mV s^{-1}. Electrochemical impedance (EIS, 100 kHz to 0.01 Hz) was performed in the same electrochemical workstation.

3 Results and discussions

The morphologies of $Zn_{0.76}Co_{0.24}S$ nanospheres and $Zn_{0.76}Co_{0.24}S$@N/S-rGO composite were investigated via scanning electron microscope (SEM) and transmission electron microscope (TEM). The size of $Zn_{0.76}Co_{0.24}S$ nanospheres (Figure S1) is obviously larger than that of $Zn_{0.76}Co_{0.24}S$@N/S-rGO, which implies that the introduction of graphene could limit the size of nanospheres. Compared with pure $Zn_{0.76}Co_{0.24}S$ nanospheres, the SEM images of $Zn_{0.76}Co_{0.24}S$@N/S-rGO show that the uniform nanospheres with an average size of 200 nm are anchored on RGO sheet (Figure 1a and b). Furthermore, the interaction of functional groups on rGO and $Zn_{0.76}Co_{0.24}S$ nanospheres on rGO can effectively inhibit the aggregation and further growth of $Zn_{0.76}Co_{0.24}S$ nanospheres demonstrated by the TEM images (Figure 1 and Figure S1). Figure 1c shows TEM image of $Zn_{0.76}Co_{0.24}S$@N/S-rGO, which displays a perfect hollow-structured $Zn_{0.76}Co_{0.24}S$ nanosphere tightly anchored on rGO matrix. The high-resolution TEM (HRTEM) image of $Zn_{0.76}Co_{0.24}S$@N/S-rGO composites in Figure 1d indicates that the $Zn_{0.76}Co_{0.24}S$ nanospheres are well-dispersed on the rGO nanosheet and the lattice spacings of 0.312 and 0.269 nm correspond to the (111) and (200) planes of $Zn_{0.76}Co_{0.24}S$@N/S-rGO.

In order to further investigate the crystallographic structure and graphitization degree of carbon in the as-obtained $Zn_{0.76}Co_{0.24}S$@N/S-rGO composite, XRD and Raman spectra characterization were conducted. As depicted in Figure 2a, all main diffraction peaks of $Zn_{0.76}Co_{0.24}S$@N/S-rGO and $Zn_{0.76}Co_{0.24}S$ were in good agreement with the standard patterns of $Zn_{0.76}Co_{0.24}S$ (JCPDS no. 47-1656); the peak at 28.6°, 47.6°, 56.4°, and 76.9°, respectively, which are indexed to the (111), (220), (311), and (331) planes of the cubic phase of $Zn_{0.76}Co_{0.24}S$. The sharp peaks indicate the good crystallinity of the as-obtained $Zn_{0.76}Co_{0.24}S$. The small peak at 26.5° in $Zn_{0.76}Co_{0.24}S$@N/S-rGO could be assigned to rGO. No obvious peak related to graphite can be observed in the XRD pattern of $Zn_{0.76}Co_{0.24}S$@N/S-rGO,

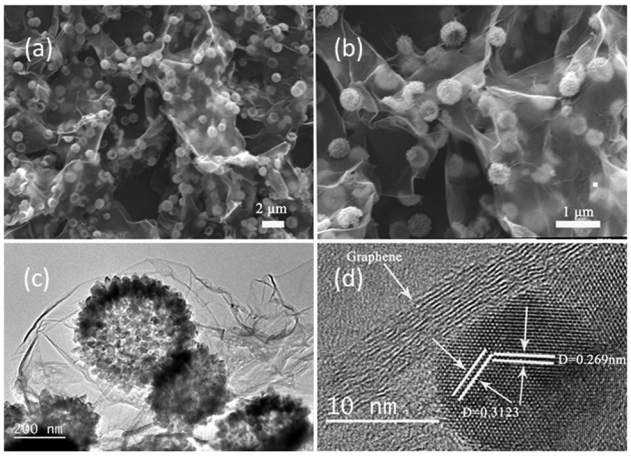

Figure 1: (a) Low and (b) high magnification SEM images of $Zn_{0.76}Co_{0.24}S$@N/S-rGO. (c) TEM images of $Zn_{0.76}Co_{0.24}S$@N/S-rGO. (d) HRTEM image of $Zn_{0.76}Co_{0.24}S$@N/S-rGO.

indicating amorphous carbon in the composite. Moreover, the content of $Zn_{0.76}Co_{0.24}S$ in $Zn_{0.76}Co_{0.24}S$@N/S-rGO is calculated to be around 67% in terms of the result of thermogravimetric analysis (Figure S2) [18]. The energy-dispersive X-ray spectroscopy of $Zn_{0.76}Co_{0.24}S$@N/S-rGO shown in Figure S3 indicates that the element of Zn, Co, and S are present in the sample, which confirms that the composite was $Zn_{0.76}Co_{0.24}S$. Meanwhile, the EDX mapping images of Zn, Co, S, and C elements distinctly demonstrate the uniform distribution of the elements in the hollow nanospheres on GO nanosheet (Figure S4). The Raman spectra of $Zn_{0.76}Co_{0.24}S$@N/S-rGO and GO samples are given in Figure 2b to better understand the surface layer of $Zn_{0.76}Co_{0.24}S$@N/S-rGO. The broad band located around 1,590 cm^{-1} corresponds to the E_2g symmetric vibrational mode of graphite-type sp^2 carbons. The broad band around 1,350 cm^{-1} is an indicator of structural disorder, which is characterized by bond angle distribution and linked with sp^3 carbons [19]. The Raman spectra further confirm the residual carbon in the $Zn_{0.76}Co_{0.24}S$ nanospheres, which is generated from the carbonization of organic molecules in the annealing process.

The Brunauer–Emmett–Teller (BET) analysis was carried out to evaluate the structural feature and porosity of $Zn_{0.76}Co_{0.24}S$@N/S-rGO and $Zn_{0.76}Co_{0.24}S$. The nitrogen adsorption–desorption isotherms and pore-size distribution curves of $Zn_{0.76}Co_{0.24}S$@N/S-rGO and $Zn_{0.76}Co_{0.24}S$ are shown in Figure 3a and b, respectively. The BET-specific surface area was measured to be 40.9 $m^2 g^{-1}$ for $Zn_{0.76}Co_{0.24}S$@N/S-rGO and 25.2 $m^2 g^{-1}$ for $Zn_{0.76}Co_{0.24}S$. The nitrogen adsorption–desorption isotherm of $Zn_{0.76}Co_{0.24}S$@N/S-rGO was found to coincide with type IV BET classification [20]. As the pore-size distribution curve shows, the pores of $Zn_{0.76}Co_{0.24}S$@N/S-rGO were mostly mesopores within 10 nm so that it could provide short and easy diffusion pathways for electrolyte ions to improve their electrochemical performance [21]. On the contrary, there were hardly any mesopores in $Zn_{0.76}Co_{0.24}S$.

X-ray photoemission spectroscopy (XPS) measurements were carried out to further study the chemical composition and valence states of $Zn_{0.76}Co_{0.24}S$@N/S-rGO. XPS survey spectra of the $Zn_{0.76}Co_{0.24}S$@N/S-rGO identify the existence of Zn, Co, S, and C elements without any impurities (Figure 4a). The spectrum shows two peaks at 1,022.6 and 1,045.6 eV which can be assigned to Zn $2p_{3/2}$ and Zn $2p_{1/2}$, respectively, indicating the existence of Zn^{2+} (Figure 4b) [22]. The biding energy at 780.6 and 796.5 eV can be assigned to the $2p_{3/2}$ and $2p_{1/2}$ of Co^{2+}, demonstrating the coexistence of Co^{3+} and Co^{2+} in the sample [23]. Two peaks can be discovered from the S 2p

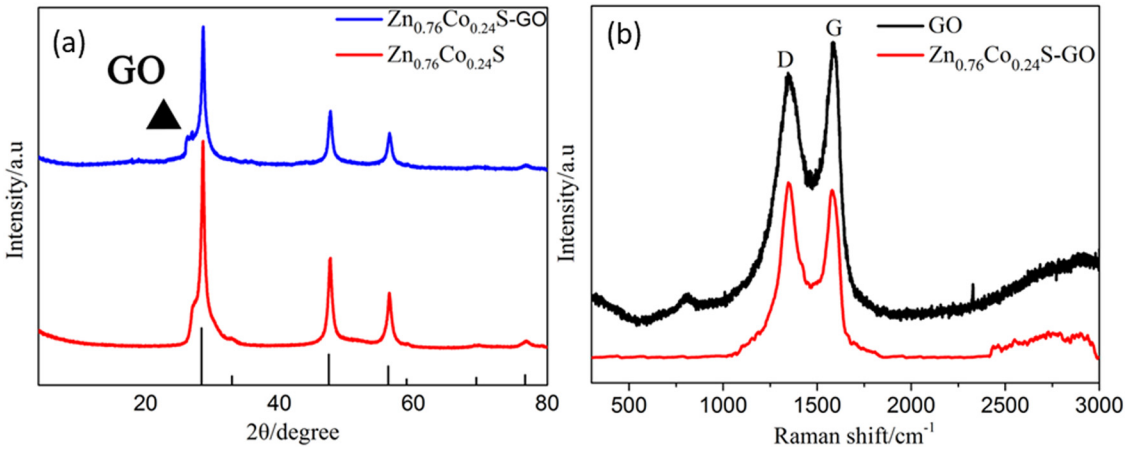

Figure 2: (a) XRD patterns of the $Zn_{0.76}Co_{0.24}S$@N/S-rGO and (b) Raman spectra of GO and $Zn_{0.76}Co_{0.24}S$@N/S-rGO.

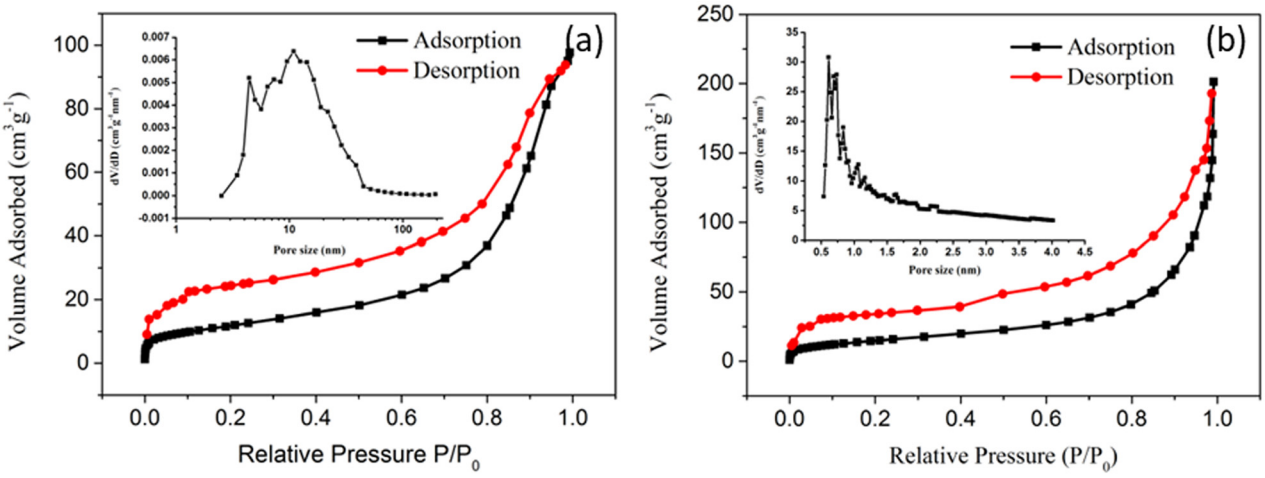

Figure 3: (a) N_2-sorption-isotherms and corresponding pore-size distribution of the (a) $Zn_{0.76}Co_{0.24}S$@N/S-rGO and (b) $Zn_{0.76}Co_{0.24}S$.

spectrum in Figure 4d. The peak at 162.5 eV is a typical metal-sulfur bond in metal sulfides [24], while another peak at 169.0 eV is ascribed to sulfur oxides [25]. The C 1s HR-XPS spectrum shows four peaks located at 286.4, 285.4, 284.82, and 284.78 eV, which ascribed to the C=O, C–O, C–S, and C–C bonds, respectively [26]. Besides, after the hydrothermal reaction, rGO is not completely reduced because of the existence of O=C–O and C–O bonds. Due to the existence of C–S–C bond, it can act as the conjunction between the rGO and $Zn_{0.76}Co_{0.24}S$, resulting in the formation of a stable $Zn_{0.76}Co_{0.24}S$@N/S-rGO structure [27]. Moreover, the doped S atom changes the local charge distribution, which will enhance the local electron transfer, and thus, increase the electronic conductivity of the composite [28]. Figure 3f depicts the HR-XPS spectrum of N 1s of $Zn_{0.76}Co_{0.24}S$@N/S-rGO with three peaks: pyrrolic-type N (399.0 eV), pyrrolic N (399.9 eV), and graphitic N (401.5 eV), demonstrating the existence of N element in $Zn_{0.76}Co_{0.24}S$@N/S-rGO [29].

To investigate the electrochemical performance of $Zn_{0.76}Co_{0.24}S$@N/S-rGO as anodes for LIBs, cyclic voltammograms (CV) curves of the $Zn_{0.76}Co_{0.24}S$@N/S-rGO electrodes

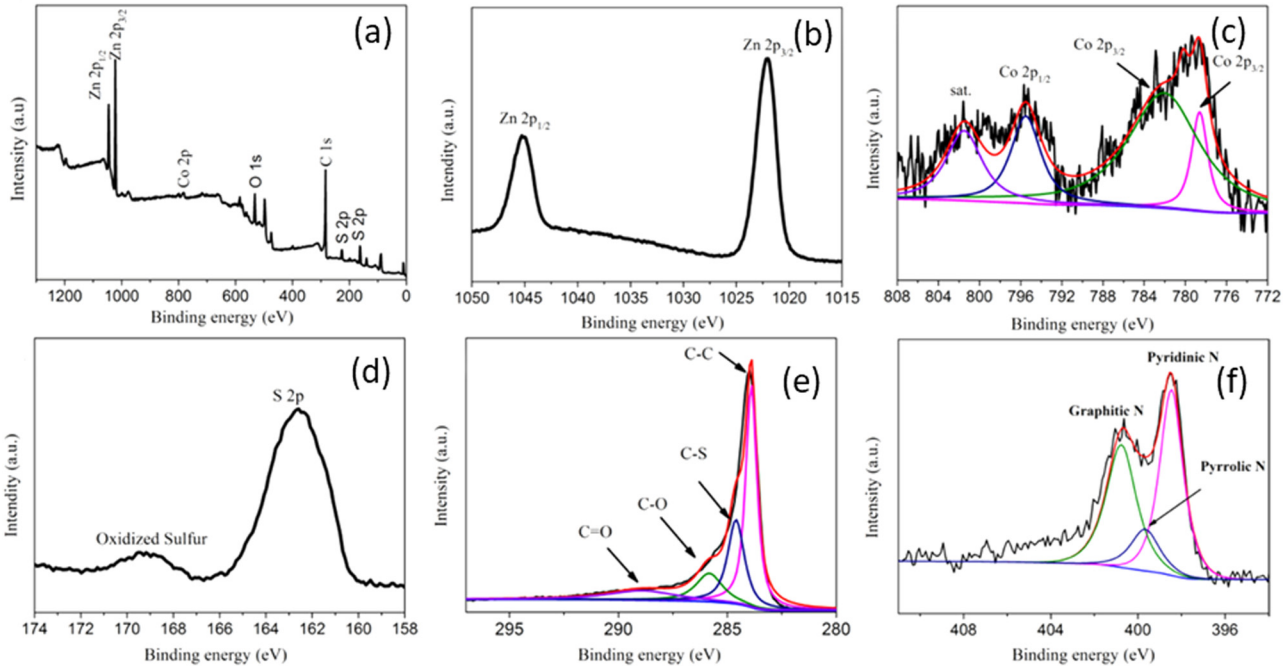

Figure 4: XPS spectra of the as-synthesized $Zn_{0.76}Co_{0.24}S$@N/S-rGO: (a) survey, (b) Zn 2p, (c) Co 2p, (d) S 2p, (e) C 1s, and (f) N 1s.

were first carried out at a scan rate of 0.1 mV s^{-1} between 0.01–3.0 V. As illustrated in Figure 5a, two peaks centered at 0.5 and 0.2 V in the first cathodic scan correspond to the reduction of $Zn_{0.76}Co_{0.24}S$ to Zn and Co nanocrystals, accompanied with an irreversible reaction related to the formation of the solid electrolyte interphase (SEI) layer on the surface of the electrode [30]. During anodic scan, the peaks at 1.3 and 0.15 V are attributed to the oxidation of Zn and Co [31]. The second and third CV curves of the $Zn_{0.76}Co_{0.24}S$@N/S-rGO electrode almost overlap with each other, which imply the superior stability and excellent reversibility of the redox reactions of the $Zn_{0.76}Co_{0.24}S$@N/S-rGO electrode [32].

The typical galvanostatic discharge–charge voltage profiles of the $Zn_{0.76}Co_{0.24}S$@N/S-rGO electrode at the current density of 0.1 A g^{-1} within the voltage range of 0.01–3.0 V (versus $Li/Li^{+)}$ are shown in Figure 5b. The $Zn_{0.76}Co_{0.24}S$@N/S-rGO electrode exhibits an initial discharge and charge capacity of 1,346 and 872.2 mA h g^{-1}, respectively. The irreversible capacity of the $Zn_{0.76}Co_{0.24}S$@N/S-rGO electrode observed in the first cycle would be attributed to the formation of SEI layer and some irreversible reaction happened at the phase between metal and Li_2S which leads to an exceptional Li consumption [33]. In addition, other reasons can also contribute to the irreversible capacity, e.g. some oxygen-containing functional groups on GO nanosheet can consume Li^+ during cycling [34]. For comparison, $Zn_{0.76}Co_{0.24}S$ shows a lower CE of about 51% (see Figure S5). This is mainly caused by the larger morphology degradation of the electrode without GO protection during the discharge process [35]. The discharge capacities of the $Zn_{0.76}Co_{0.24}S$@N/S-rGO electrode at the second and third cycles are 1000.9 and 930.5 mA h g^{-1}, respectively. A high gravimetric capacity of 750.6 mA h g^{-1} could still be maintained by the $Zn_{0.76}Co_{0.24}S$@N/S-rGO electrode over 100 cycles (Figure S6).

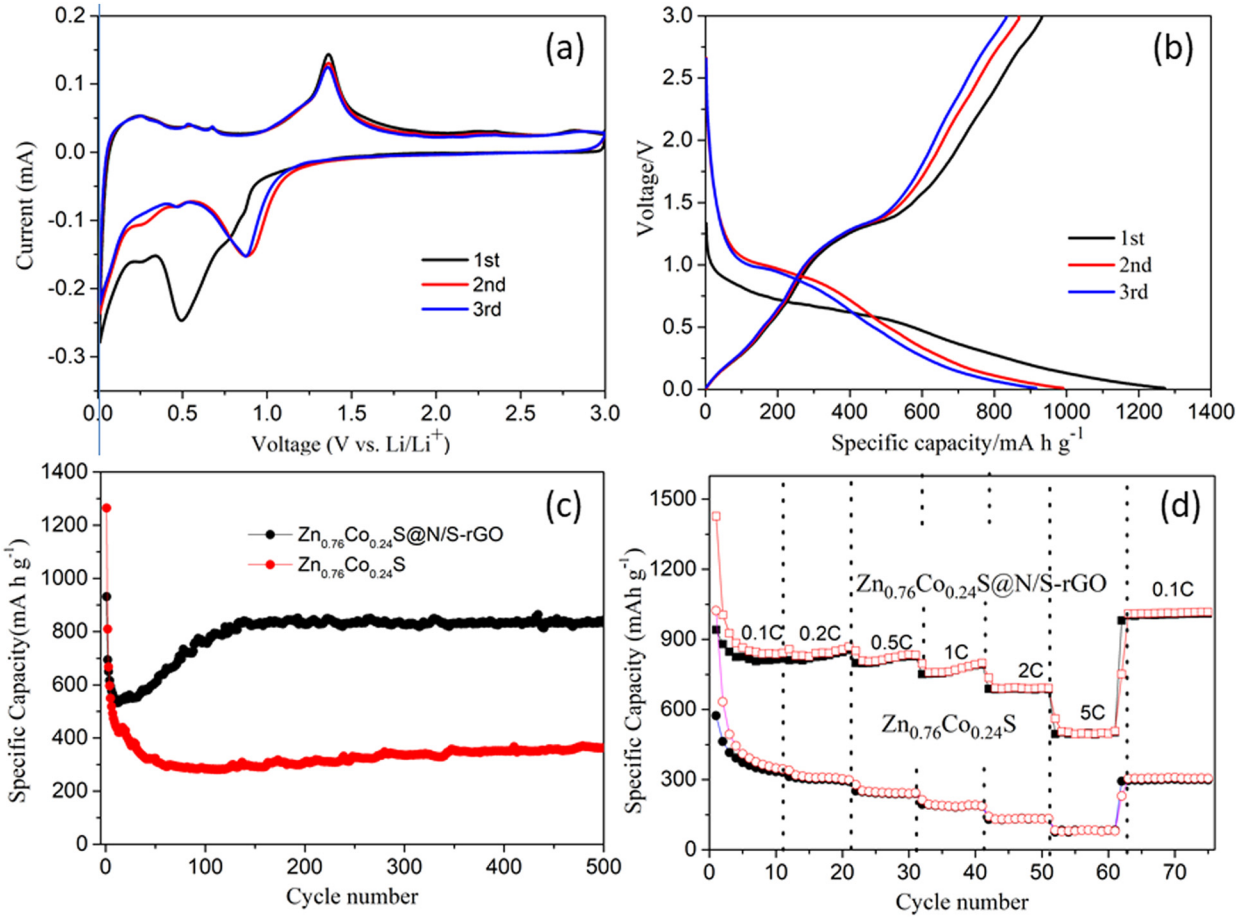

Figure 5: Lithium ion storage behaviours of $Zn_{0.76}Co_{0.24}S$@N/S-rGO and $Zn_{0.76}Co_{0.24}S$ composite electrodes: (a) cyclic voltammetry curves of $Zn_{0.76}Co_{0.24}S$@N/S-rGO between 0.01 and 3 V with a scan rate of 0.1 mV s^{-1}; (b) charge/discharge voltage profiles of $Zn_{0.76}Co_{0.24}S$@N/S-rGO at a rate of 0.1 A g^{-1}; (c) cycling performance of the two different materials at a current density of 1 A g^{-1}; and (d) rate performance of two different electrodes.

In order to reveal superior Li^+ storage properties of $Zn_{0.76}Co_{0.24}S$@N/S-rGO and $Zn_{0.76}Co_{0.24}S$, the cycle stability of the composites was further evaluated at a current density of 1.0 A g^{-1} for 500 cycles (Figure 5c). Obviously, $Zn_{0.76}Co_{0.24}S$@N/S-rGO electrode can deliver a high capacity of 1,280 mA h g^{-1} in the first cycle, while $Zn_{0.76}Co_{0.24}S$ only delivers 980 mA h g^{-1}. Even after 50 cycles at 1.0 A g^{-1}, the $Zn_{0.76}Co_{0.24}S$@N/S-rGO electrodes can still deliver high reversible discharge capacities of 804 mA h g^{-1}. However, the reversible capacities of $Zn_{0.76}Co_{0.24}S$ decrease quickly from 700 (next cycle) to 300 mA h g^{-1} (500th cycles). It could be easy to explain that the $Zn_{0.76}Co_{0.24}S$ nanospheres anode suffer serious volume pulverization during the discharge/charge process, which can result in a rapidly capacity fading. The reason why the capacity raised during the cycling has been evaluated in the previous literature, like transition metal oxides or sulphides [36]. It can be concluded from the result that $Zn_{0.76}Co_{0.24}S$ anchored on graphene can extremely enhance the cycling performance. On the one hand, the layered structured of rGO can provide the reversible capacity, which is beneficial for the diffusion of Li^+ ions. On the other hand, the rGO can effectively buffer the volume change during cycling [37].

The rate capabilities of the $Zn_{0.76}Co_{0.24}S$@N/S-rGO and $Zn_{0.76}Co_{0.24}S$ electrodes are presented in Figure 5d. The $Zn_{0.76}Co_{0.24}S$@N/S-rGO electrode delivers excellent reversible discharge capacities of 925, 850, 837, 808, 758, and 690 mA h g^{-1} at current densities of 0.1, 0.2, 0.5, 1, 2, and 5 A g^{-1}, respectively. When the current density was restored to 0.1 A g^{-1}, a high reversible capacity of 1,014 mA h g^{-1} could be achieved, indicating excellent rate capacity of the $Zn_{0.76}Co_{0.24}S$@N/S-rGO electrode. In contrast, the discharge capacities of $Zn_{0.76}Co_{0.24}S$ nanosphere decreased dramatically when we raise the current density from 0.1 to 5 A g^{-1}. The excellent rate capability of $Zn_{0.76}Co_{0.24}S$@N/S-rGO is originated from its unique structure [38]. First, the introduction of hollow $Zn_{0.76}Co_{0.24}S$ nanospheres could expand the intervals of GO layers, which is beneficial for the interfacial compatibility and fast ion transfer [39]. Second, the size of the $Zn_{0.76}Co_{0.24}S$ spheres was greatly reduced by their interactions with rGO providing more active site for Li storage [40].

Meanwhile, to further explore charge-transfer kinetics and interfacial resistance, the electrochemical EIS is conducted. Figure S6 shows the typical Nyquist plot of $Zn_{0.76}Co_{0.24}S$@N/S-rGO and $Zn_{0.76}Co_{0.24}S$ electrodes before cycling. The high frequency semi-circle represents the charge transfer resistance (R_{ct}), while the slope in the low frequency region indicates the Warburg impedance [41]. The R_e and R_{ct} values of the $Zn_{0.76}Co_{0.24}S$@N/S-rGO electrode are significantly smaller than the corresponding values of the $Zn_{0.76}Co_{0.24}S$ electrode, suggesting that the $Zn_{0.76}Co_{0.24}S$@N/S-rGO electrodes have lower ohmic resistance and faster faradic reaction kinetics than the $Zn_{0.76}Co_{0.24}S$ electrode [42]. Furthermore, the graphene framework-supported $Zn_{0.76}Co_{0.24}S$ could further decrease the electrical resistance, which is beneficial for the performance of LIBs [43].

In order to study the electrochemical properties of $Zn_{0.76}Co_{0.24}S$@N/S-rGO as anode for SIBs, the materials were evaluated in coin-type half cells at room temperature. The CV curves of the $Zn_{0.76}Co_{0.24}S$@N/S-rGO electrode at 0.1 mV s^{-1} are shown in Figure 6a. During the 1st cathodic process, three cathodic peaks located at 0.2, 0.3, and 0.6 V were observed; these peaks corresponded to the insertion of sodium ions into $Zn_{0.76}Co_{0.24}S$@N/S-rGO lattice to form $Na_xZn_{0.76}Co_{0.24}S$@N/S-rGO, conversion reactions of $Zn_{0.76}Co_{0.24}S$@N/S-rGO into Zn and Co metallic nanoparticles embedded into amorphous Na_2S matrix, and together with the generation of SEI film because of the irreversible reactions [44]. In the reversible charge process, the anodic peaks at around 0.9 V could be attributing to the transformed form Zn to ZnS and the oxidation of Co [45]. The CV curves of the second and third cycles are almost overlapped with each other, indicating the excellent reversible sodium storage of the $Zn_{0.76}Co_{0.24}S$@N/S-rGO [46].

The typical galvanostatic discharge/charge curves of the $Zn_{0.76}Co_{0.24}S$@N/S-rGO electrode at 0.1 A g^{-1} are presented in Figure 6b. The first discharge plateau of $Zn_{0.76}Co_{0.24}S$@N/S-rGO electrode is located at around 0.6 V, corresponding to the intercalation of Na^+ into $Zn_{0.76}Co_{0.24}S$@N/S-rGO, which is consistent with the CV results (Figure 6a). The initial discharge and charge capacities of $Zn_{0.76}Co_{0.24}S$@N/S-rGO were 686.1 and 649.5 mA h g^{-1}, respectively, and the initial coulombic efficiency is 96.4%. The discharge capacity of the subsequent cycles was founded to be 625 mA h g^{-1}. The main reasons for the capacity loss of the $Zn_{0.76}Co_{0.24}S$@N/S-rGO in the first few cycles are mainly caused by the decomposition of electrolyte and development of the formation of SEI film [47]. In addition, sodium can also be consumed by the active oxygen-containing functional group in the rGO. The charge/discharge curves of second and third cycle almost overlap with each other, showing the excellent electrochemical stability and reversibility of $Zn_{0.76}Co_{0.24}S$@N/S-rGO.

Moreover, the long-term cycling of the $Zn_{0.76}Co_{0.24}S$@N/S-rGO and the $Zn_{0.76}Co_{0.24}S$ at 1 A g^{-1} are also explored and present in Figure 6c. The discharge capacity is 756 mA h g^{-1} for $Zn_{0.76}Co_{0.24}S$@N/S-rGO and 675 mA h g^{-1} for pure $Zn_{0.76}Co_{0.24}S$, which is lower than that of $Zn_{0.76}Co_{0.24}S$@N/

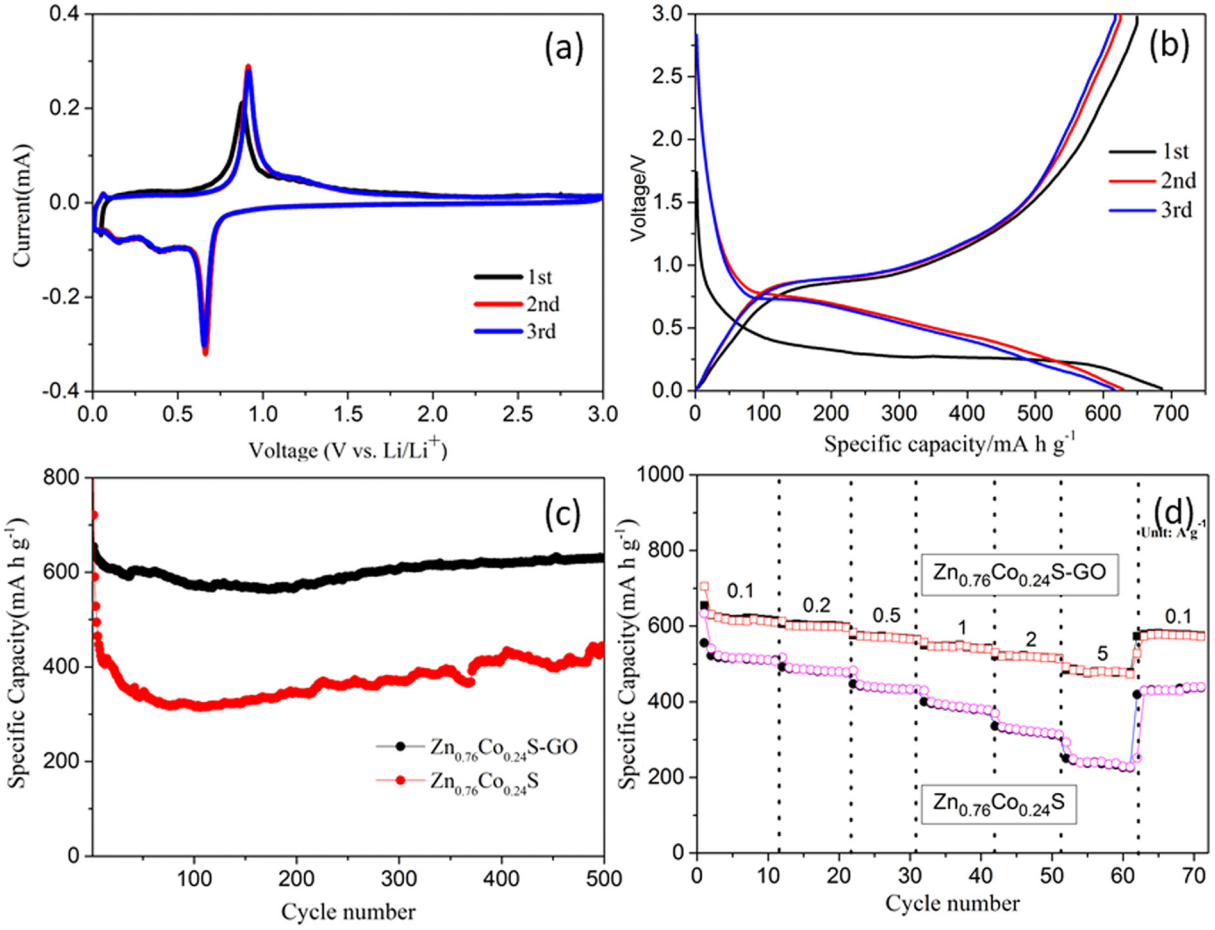

Figure 6: Electrochemical performance of $Zn_{0.76}Co_{0.24}S$@N/S-rGO as anodes for SIBs (a) CV curves of $Zn_{0.76}Co_{0.24}S$@N/S-rGO electrode at a scan rate of 0.1 mV s^{-1} within a potential range of 0.01–3.0 V (vs Na/Na^+). (b) Discharge/charge voltage curves of the with $Zn_{0.76}Co_{0.24}S$@N/S-rGO electrode at a current density of 1 A g^{-1}. (c) Cycling performance at current density of 1 A g^{-1}. (d) Rate capacity.

S-rGO. The discharge capacities of $Zn_{0.76}Co_{0.24}S$@N/S-rGO and $Zn_{0.76}Co_{0.24}S$ electrode for the 500th cycles are 605 and 403 mA h g^{-1}, respectively. The capacity retentions compared with first cycle are 93.1% and 51.7%. The excellent cycling stability of $Zn_{0.76}Co_{0.24}S$@N/S-rGO may be attributed to the good conductivity of rGO and the active site of hollow $Zn_{0.76}Co_{0.24}S$ nanospheres [48]. The poor stability of $Zn_{0.76}Co_{0.24}S$ can be attributed to the structure collapse without rGO. The rate performances of $Zn_{0.76}Co_{0.24}S$@N/S-rGO and $Zn_{0.76}Co_{0.24}S$ electrodes were also investigated (Figure 6d). The $Zn_{0.76}Co_{0.24}S$@N/S-rGO electrode clearly shows much better rate capability than the $Zn_{0.76}Co_{0.24}S$ electrode. Reversible specific capacities of 614.4, 601.3, 565.5, 541.3, 516.1, and 478.5 mA h g^{-1} were obtained at current densities of 0.1, 0.2, 0.5, 1, 2, and 5 A g^{-1}, respectively. However, the discharge capacities achieved by the $Zn_{0.76}Co_{0.24}S$ electrodes were 515.3, 479.5, 433.4, 380.6, 316.3, and 237.9 mA h g^{-1} at current densities from 0.1 to 5 A g^{-1}. Particularly, despite cycling at high current density of 5 A g^{-1}, the discharge capacity of $Zn_{0.76}Co_{0.24}S$@N/S-rGO can still reach 478.5 mA h g^{-1}, which is much higher than that of $Zn_{0.76}Co_{0.24}S$ (237.9 mA h g^{-1}). When the current density was restored to 0.1 A g^{-1}, the capacity of $Zn_{0.76}Co_{0.24}S$@N/S-rGO composites almost recovered to the initial value. The rate capabilities of the $Zn_{0.76}Co_{0.24}S$@N/S-rGO are much better than those without GO which can further confirm the superior cycling stability of the $Zn_{0.76}Co_{0.24}S$@N/S-rGO electrodes.

The advantages of the $Zn_{0.76}Co_{0.24}S$@N/S-rGO electrode in simultaneously achieving efficient Li^+/Na^+ storage are shown in Figure 7. The superior electrochemical properties can be attributed to the unique structure in exploring the accessible active sites, which can effectively improve the ion/electron transport [49]. The graphene network can protect the $Zn_{0.76}Co_{0.24}S$ nanospheres, which can increase the active sites between electrolyte and Li/Na ion. Moreover, the excellent electronic conductivity of 3D graphene network can enhance the electron

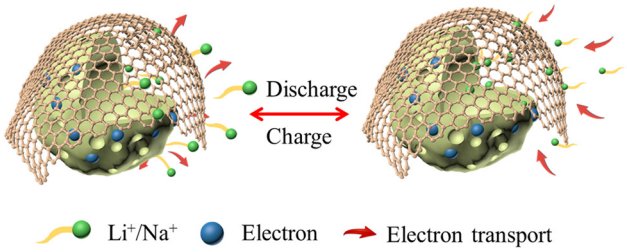

Figure 7: Schematic illustration of the enhanced ion/electron transport of the $Zn_{0.76}Co_{0.24}S$@N/S-rGO electrode.

and ion transport during the whole electrode [50]. As a result, $Zn_{0.76}Co_{0.24}S$ nanospheres integrating graphene network, hollow $Zn_{0.76}Co_{0.24}S$ nanospheres, and 3D graphene synergistically enhance the electrochemical performance.

4 Conclusion

In summary, rGO-supported hollow $Zn_{0.76}Co_{0.24}S$ nanospheres composite has been successfully synthesized through an effective hydrothermal method followed by freeze-drying and calcination. The rGO matrix can increase the conductivity of the hybrid materials, as well as tolerate the fast ion intercalation and extraction of electrodes during cycling process. Meanwhile, the encapsulated hollow $Zn_{0.76}Co_{0.24}S$ nanospheres can provide more active sites and are beneficial for the transportation of Li/Na ions, which can give rise to the high rate capacity and excellent performance. Benefited from the smart structural and compositional features, $Zn_{0.76}Co_{0.24}S$@N/S-rGO-based LIBs and SIBs exhibit high initial discharge capacities, excellent rate capability, and stable cycling performance. As a result, $Zn_{0.76}Co_{0.24}S$@N/S-rGO exhibits a high reversible capacity of 605 mA h g^{-1} for SIBs at 1 A g^{-1} over 500 cycles. Specifically, even at a high rate of 5 A g^{-1}, the capacities of LIBs and SIBs can still retain 690 and 478.5 mA h g^{-1}, respectively. These superior Li/Na storage performances of $Zn_{0.76}Co_{0.24}S$@N/S-rGO make it promising anode materials for both LIBs and SIBs.

Acknowledgements: This work was supported by National Natural Science Foundation of China (51673117, 52003111), The Key R&D Programme of Guangdong Province (2019B010929002)

Conflict of interest: The authors declare no conflict of interest regarding the publication of this paper.

References

[1] Kumar A, Ciucci F, Morozovska AN, Kalinin SV, Jesse S. Measuring oxygen reduction/evolution reactions on the nanoscale. Nat Chem. 2011;3(9):707–13.
[2] Jia F, Li G, Yang B, Yu B, Shen Y, Cong H. Investigation of rare earth upconversion fluorescent nanoparticles in biomedical field. Nanotechnol Rev. 2019;8(1):1–17.
[3] Goodenough JB, Park K-S. The Li-ion rechargeable battery: a perspective. J Am Chem Soc. 2013;135(4):1167–76.
[4] Kapaev RR, Novikova1 SA, Chekannikov AA, Skundin AM, Gryzlov DY, Yaroslavtsev AB. Effect of carbon source and synthesis conditions on the $LiFePO_4$/C cathode properties. Rev Adv Mater Sci. 2018;57(5):183–92.
[5] Reddy MV, Rao Subba GV, Chowdari BVR. Metal oxides and oxysalts as anode materials for Li ion batteries. Chem Rev. 2013;113(7):5364–457.
[6] Liu Y, Jiang L, Wang H, Wang H, Jiao W, Chen G, et al. A brief review for fluorinated carbon: synthesis, properties and applications. Nanotechnol Rev. 2019;8(1):573–86.
[7] Liu B, Liu H, Liang M, Liu L, Lv Z, Zhou H, et al. Controlled synthesis of hollow octahedral ZnCo2O4 nanocages assembled from ultrathin 2D nanosheets for enhanced lithium storage. Nanoscale. 2017;9(44):17174–80.
[8] Ventrapragada LK, Creager SE, Rao AM, Podila R. Carbon nanotubes coated paper as current collectors for secondary Li-ion batteries. Nanotechnol Rev. 2019;8(1):18–23.
[9] Huang J, Wu B, Lyu S, Li T, Han H, Li D, et al. Improving the thermal energy storage capability of diatom-based biomass/polyethylene glycol composites phase change materials by artificial culture methods. Sol Energy Mater Sol Cell. 2021;219(3):110797.
[10] Lin Y, Qiu Z, Li D, Ullah S, Hai Y, Xin H, et al. NiS_2@CoS_2 nanocrystals encapsulated in N-doped carbon nanocubes for high performance lithium/sodium ion batteries. Energy Storage Mater. 2018;11(3):67–74.
[11] Zhao X, Zhao T, Peng X, Yang L, Shu Y, Jiang T, et al. In situ synthesis of expanded graphite embedded with amorphous carbon-coated aluminum particles as anode materials for lithium-ion batteries. Nanotechnol Rev. 2020;9(1):436–44.
[12] Liang Y, Li Y, Wang H, Zhou J, Wang J, Regier T, et al. Co_3O_4 nanocrystals on graphene as a synergistic catalyst for oxygen reduction reaction. Nat Mater. 2011;10(10):780–6.
[13] Li Z, Xu K, Pan Y. Recent development of supercapacitor electrode based on carbon materials. Nanotechnol Rev. 2019;8(1):35–49.
[14] Jiang H, Ren D, Wang H, Hu Y, Guo S, Yuan H, et al. 2D Monolayer MoS_2-carbon interoverlapped superstructure: engineering ideal atomic interface for lithium ion storage. Adv Mater. 2015;27(24):3687–95.
[15] Symes MD, Cronin L. Decoupling hydrogen and oxygen evolution during electrolytic water splitting using an electron-coupled-proton buffer. Nat Chem. 2013;5(5):403–9.
[16] Dash CS, Prabaharan SRS. Nano resistive memory (Re-RAM) devices and their applications. Rev Adv Mater Sci. 2019;58(1):248–70.
[17] Xiang X, Zhang K, Chen J. Recent advances and prospects of cathode materials for sodium-ion batteries. Adv Mater. 2015;27(36):5343–64.

[18] Yu L, Yang JF, Lou XWD. Formation of CoS_2 nanobubble hollow prisms for highly reversible lithium storage. Angew Chem Int Ed. 2016;55(43):13422–6.
[19] Crabtree G. Perspective: the energy-storage revolution. Nature. 2015;526(7575):S92.
[20] Liu X, Zhang K, Lei K, Li F, Tao Z, Chen J. Facile synthesis and electrochemical sodium storage of CoS2 micro/nano-structures. Nano Res. 2016;9(1):198–206.
[21] Park GD, Kim JH, Park S-K, Kang YC. MoSe2 embedded CNT-reduced graphene oxide composite microsphere with superior sodium ion storage and electrocatalytic hydrogen evolution performances. ACS Appl Mater Interfaces. 2017;9(12):10673–83.
[22] Dong Y, Yang S, Zhang Z, Lee J-M, Zapien JA. Enhanced electrochemical performance of lithium ion batteries using Sb_2S_3 nanorods wrapped in graphene nanosheets as anode materials. Nanoscale. 2018;10(7):3159–65.
[23] Li Z, Xu K, Wei F. Recent progress in photodetectors based on low-dimensional nanomaterials. Nanotechn Rev. 2018;7(5):393–411.
[24] Liu C, Li F, Ma L-P, Cheng H-M. Advanced materials for energy storage. Adv Mater. 2010;22(8):E28–62.
[25] Su Q, Xie J, Zhang J, Zhong Y, Du G, Xu B. *In situ* transmission electron microscopy observation of electrochemical behaviour of CoS2 in lithium-ion battery. ACS Appl Mater Interfaces. 2014;6(4):3016–22.
[26] Choi SH, Ko YN, Lee J-K, Kang YC. 3D MoS2-graphene microspheres consisting of multiple nanospheres with superior sodium ion storage properties. Adv Funct Mater. 2015;25(12):1780–8.
[27] Kundu D, Talaie E, Duffort V, Nazar LF. The emerging chemistry of sodium ion batteries for electrochemical energy storage. Angew Chem Int Ed. 2015;54(11):3431–48.
[28] Lin Y, Guo X, Hu M, Liu B, Dong Y, Wang X, et al. A MoS_2@SnS heterostructure for sodium-ion storage with enhanced kinetics. Nanoscale. 2020;12(27):14689–98.
[29] Zhou Y, Yan D, Xu H, Feng J, Jiang X, Yue J, et al. Hollow nanospheres of mesoporous Co9S8 as a high-capacity and long-life anode for advanced lithium ion batteries. Nano Energy. 2015;12(5):528–37.
[30] Fang Y, Yu XY, Lou XWD. Bullet-like Cu_9S_5 hollow particles coated with nitrogen-doped carbon for sodium-ion batteries. Angew Chem Int Ed. 2019;58(23):7744–8.
[31] Tang Y, Zhao Z, Hao X, Wang Y, Liu Y, Hou Y, et al. Engineering hollow polyhedrons structured from carbon-coated $CoSe_2$ nanospheres bridged by CNTs with boosted sodium storage performance. J Mater Chem A. 2017;5(26):13591–600.
[32] Wang C, Lan M, Zhang Y, Bian H, Yuen M-F, Ostrikov K, et al. Fe1-xS/C nanocomposites from sugarcane waste-derived microporous carbon for high-performance lithium ion batteries. Green Chem. 2016;18(10):3029–39.
[33] Xu Y, Li W, Zhang F, Zhang X, Zhang W, Lee C-S, et al. In situ incorporation of FeS nanoparticles/carbon nanosheets composite with an interconnected porous structure as a high-performance anode for lithium ion batteries. J Mater Chem A. 2016;4(10):3697–703.
[34] Fan H, Yu H, Zhang Y, Zheng Y, Luo Y, Dai Z, et al. Fe-Doped Ni_3C nanodots in N-doped carbon nanosheets for efficient hydrogen-evolution and oxygen-evolution electrocatalysis. Angew Chem Int Ed. 2017;56(41):12566–70.
[35] Wu A, Tian C, Yan H, Jiao Y, Yan Q, Yang G, et al. Hierarchical MoS_2@MoP core–shell heterojunction electrocatalysts for efficient hydrogen evolution reaction over a broad pH range. Nanoscale. 2016;8(21):11052–9.
[36] Qiu Z, Lin Y, Xin H, Han P, Li D, Yang B, et al. Ultrahigh level nitrogen/sulfur co-doped carbon as high performance anode materials for lithium-ion batteries. Carbon. 2018;126(3):85–92.
[37] Fan L, Li B, Rooney DW, Zhang N, Sun K. In situ preparation of 3D graphene aerogels@hierarchical Fe_3O_4 nanoclusters as high rate and long cycle anode materials for lithium ion batteries. Chem Commun. 2015;51(9):1597–600.
[38] Yin X, Tang C, Chen M, Adams S, Wang H, Gong H. Hierarchical porous Cu_2ZnSnS_4 films for high-capacity reversible lithium storage applications. J Mater Chem A. 2013;1(27):7927–32.
[39] Jing M, Chen Z, Li Z, Li F, Chen M, Zhou M, et al. Facile synthesis of ZnS/N,S co-doped carbon composite from zinc metal complex for high-performance sodium-ion batteries. ACS Appl Mater Interface. 2018;10(1):704–12.
[40] Dong Y, Hu M, Zhang Z, Zapien JA, Wang X, Lee J-M, et al. nitrogen-doped carbon-encapsulated antimony sulfide nanowires enable high rate capability and cyclic stability for sodium-ion batteries. ACS Appl Nano Mater. 2019;2(3):1457–65.
[41] Liang Y-J, Yu H, Feng G, Zhuang L, Xi W, Ma M, et al. High-performance poly(lactic-*co*-glycolic acid)-magnetic microspheres prepared by rotating membrane emulsification for transcatheter arterial embolization and magnetic ablation in VX_2 liver tumors. ACS Appl Mater Interfaces. 2017;9(50):43478–89.
[42] Ji X, Herle PS, Rho Y, Nazar LF. Carbon/MoO_2 composite based on porous semi-graphitized nanorod assemblies from in situ reaction of tri-block polymers. Chem Mater. 2007;19(3):374–83.
[43] Dahn JR, Zheng T, Liu Y, Xue JS. Mechanisms for lithium insertion in carbonaceous materials. Science. 1995;270(5236):590–5.
[44] Huang J, Lin Y, Yu J, Li D, Du J, Yang B, et al. N-doped foam flame retardant polystyrene derived porous carbon as an efficient scaffold for lithium-selenium battery with long-term cycling performance. Chem Eng J. 2018;350(5):411–8.
[45] Ossai CI, Raghavan N. Nanostructure and nanomaterial characterization, growth mechanisms, and applications. Nanotechnol Rev. 2018;7(2):209–31.
[46] Wang H, Cui L-F, Yang Y, Sanchez Casalongue H, Robinson, JT, Liang Y, et al. Mn_3O_4-Graphene hybrid as a high-capacity anode material for lithium ion batteries. J Am Chem Soc. 2010;132(40):13978–80.
[47] Yoo E, Kim J, Hosono E, Zhou H-s, Kudo T, Honma I. Large reversible Li storage of graphene nanosheet families for use in rechargeable lithium ion batteries. Nano Lett. 2008;8(8):2277–82.
[48] Wang Q, Zou R, Xia W, Ma J, Qiu B, Mahmood A, et al. Facile Synthesis of Ultrasmall CoS_2 nanoparticles within thin N-doped porous carbon shell for high performance lithium-ion batteries. Small. 2015;11(21):2511–7.
[49] Wen Y, He K, Zhu Y, Han F, Xu Y, Matsuda I, et al. Expanded graphite as superior anode for sodium-ion batteries. Nat Commun. 2014;5:4033.
[50] Park C-M, Kim J-H, Kim H, Sohn H-J. Li-Alloy based anode materials for Li secondary batteries. Chem Soc Rev. 2010;39(6):3115–41.